Jan-Philipp Koester (Autor)

Design, simulation and analysis of laterally-longitudinally non-uniform edge-emitting GaAs-based diode lasers

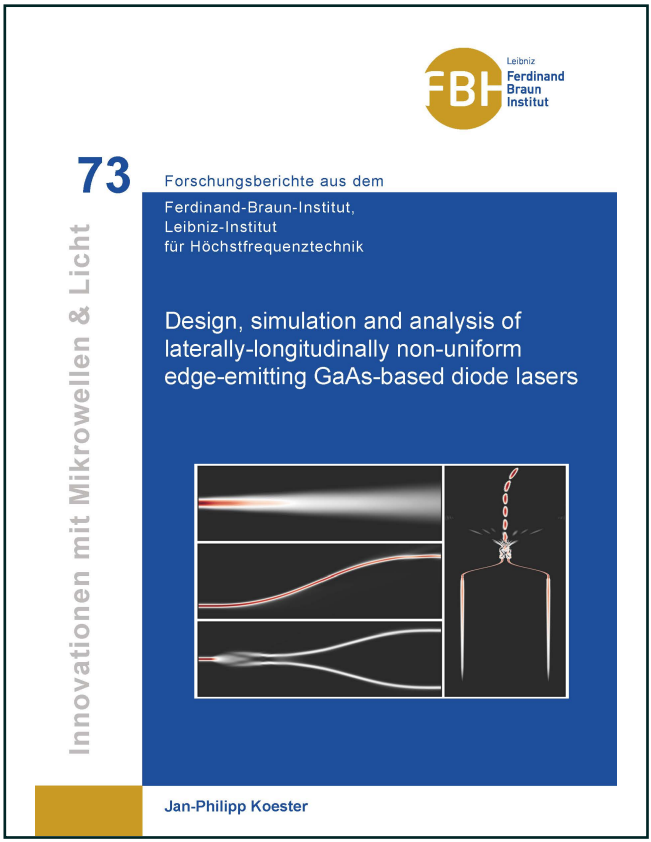

https://cuvillier.de/de/shop/publications/8893

Chapter 1

Introduction and background

In this thesis, GaAs-based edge-emitting diode lasers possessing a lateral design whose changes in longitudinal direction were investigated. This was done by comparing the results of simulations with those of experiments. In this chapter, the reader is introduced to the motivation and idea behind this work.

Edge-emitting GaAs-based diode laser

The realization of the first laser diodes was reported in 1962 by several groups, only two years after Theodore H. Maiman built the world's first laser at Hughes Research Laboratories [1–4]. These GaAs and GaAsP-based homojunction lasers suffered from high optical losses. Consequently, the devices had to be cooled and could only be operated in pulsed mode. However, several advances in the epitaxial compound semiconductors growth first enabled the realization of GaAs/AlGaAs double heterostructure-based lasers in 1970, enabling continuous-wave (CW) operation at room temperature, and subsequently, the development of quantum well-based separate confinement heterostructure lasers [5, 6].

A further significant leap towards high-performance GaAs-based diode lasers was achieved with the introduction of strained quantum wells. The strain is introduced by slight lattice constant differences in the order of 1 % of a thin layer to its surrounding material. If the corresponding layer thickness is restricted to a few nm no dislocations form. The resulting strained quantum wells show an increased differential gain, a decreased transparency carrier density leading to lower laser thresholds, as well as a better polarization mode selectivity [7–9]. In addition, the use of strain enabled to engineer the emission wavelength of GaAs-based lasers from 630 nm to 1180 nm using a variety of different quantum well materials [10]. This wavelength range is of interest for a large number of applications which includes their use as pump lasers of fiber and solid-state laser systems [11–13], as sources of LIDAR systems [14], or for direct material processing [15–18]. Further typical applications of GaAs-based diode lasers are in the context of free-space communication, the generation of terahertz radiation [19, 20], as well as the excitation of specific atomic transitions as needed to realize optical clocks [21, 22], and in spectroscopic measurements [23, 24].

A schematic representation of a typical edge-emitting GaAs-based diode laser with separate confinement heterostructure is depicted in Fig. 1.1. In the vertical (y) direction, light is guided through epitaxially grown waveguide core and cladding layers

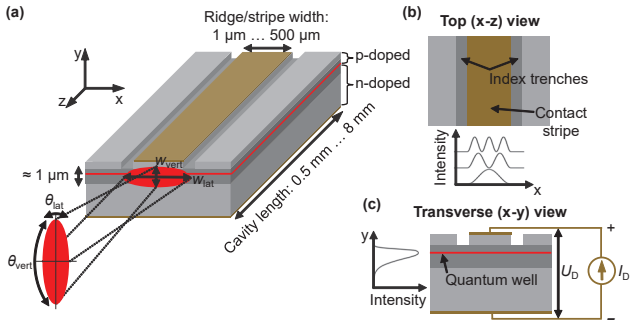

Figure 1.1: Schematic (a) three-dimensional representation of an edge-emitting diode laser including information on typical device extensions. In addition, the resulting radiation behavior including its defining parameters is shown. Panel (a) and (b) show the corresponding lateral-longitudinal (x-z) top view and a lateral-vertical (x-y) transverse cross-section, respectively.

consisting of different material compositions (e.g. Al fraction in AlGaAs). In contrast, the excess carriers, which are the basis of the optical gain, are vertically confined in several nm thick quantum wells. In longitudinal (z) direction, the laser cavity is formed by the facets created by cleaving the GaAs-substrate along appropriated crystallographic planes. Consequently, the optical feedback of the laser facets is a result of the reflection at the crystal-air interfaces. The lateral (x) confinement of the optical field can be obtained by means of gain or index guiding. The former is often accomplished by shallow or deep ion implantation. In contrast, the latter is commonly realized by etching a pair of trenches into the p-doped layers, as shown in Fig. 1.1 (a), defining a ridge waveguide.

Depending on the specific application, diode lasers must meet certain performance criteria in terms of beam quality, output power, brightness, efficiency, and spectral width. The former is commonly characterized by the beam propagation ratio $M^2 = M^2_{\mathrm{lat}} \cdot M^2_{\mathrm{vert}}$ defined as the ratio of diffraction-related beam widening experienced by the emitted field distribution compared to a Gaussian beam. Since the vertical waveguide is commonly designed to support only its fundamental mode, as indicated in Fig. 1.1 (c), the corresponding vertical beam quality is close to unity ($M^2_{\mathrm{vert}} \approx 1$). Consequently, the beam propagation ratio of diode lasers is commonly characterized by its lateral component

$$M^2_{\mathrm{lat}} = \mathrm{BPP}_{\mathrm{lat}} \frac{\pi}{\lambda_0} \qquad \text{with} \qquad \mathrm{BPP}_{\mathrm{lat}} = \frac{w_{\mathrm{lat}} \theta_{\mathrm{lat}}}{4}, \tag{1.1}$$

where w_{lat} is the lateral near-field width and θ_{lat} the corresponding far-field angle, as shown in Fig. 1.1 (a), whereas $\mathrm{BPP}_{\mathrm{lat}}$ is the lateral beam parameter product. If a high output power P_{out} is required, the contact stripe width commonly exceeds the emission wavelength multiple times, leading to the appearance of several lateral modes as indicated in panel (b) of Fig. 1.1. In this context, the lateral brightness

$$B_{\mathrm{lat}} = \frac{P_{\mathrm{out}}}{\mathrm{BPP}_{\mathrm{lat}}}, \tag{1.2}$$

which is the ratio of the output power and the beam parameter product is a suitable figure of merit. Finally, the electro-optical conversion efficiency is defined as

$$\eta_{\mathrm{eo}} = \frac{P_{\mathrm{out}}}{P_{\mathrm{el}}} \tag{1.3}$$

with $P_{\mathrm{el}} = I_{\mathrm{D}} U_{\mathrm{D}}$ being the electrical power, where I_{D} and U_{D} are the applied current and the resulting voltage across the diode, respectively.

Lateral-longitudinal non-uniform laser designs

Most GaAs-based high-power diode lasers are based on longitudinally uniform waveguide and contact stripe layouts, as schematically depicted in Fig. 1.1. Lasers that possess a width of the lateral ridge waveguide in the order of the emitted wavelength show a nearly diffraction-limited beam and are called ridge-waveguide lasers (RWL), see Fig. 1.2 (a). Depending on the emitted wavelength and vertical structure their CW output power is restricted to a few Watts [25, 26]. The factors limiting the output power are the high intra-cavity current and power densities. This causes device heating which further leads to a reduction of the internal quantum efficiency of the active region. Elevated temperatures in combination with the high optical power densities also increase the risk of catastrophic optical damage (COD) [27, 28].

Both of those effects can be reduced by increasing the contact area. Thus, higher optical output powers can be reached by increasing the ridge or contact width in the context of index- or gain-guided lasers, respectively. The resulting devices are called broad-area lasers (BAL), as schematically shown in Fig. 1.2 (b). These lasers emit up to several tens of Watts. For BALs with 90 µm wide contact, output powers of up to 25 W have been reported [29]. However, broad-area devices support a large number of lateral waveguide modes which leads to a decline of their beam quality [30].

A way to combine a good beam quality and a high output power is to use a lateral-longitudinal non-uniform laser design which combines the mode limiting narrow index-guided waveguide of an RWL and the large contact area and aperture of a BAL. This well-established device type is known as tapered laser (TL) and is schematically shown in Fig. 1.2 (c). Near diffraction-limited lateral beam characteristics at central lobe powers of up to 8 W have been demonstrated [31, 32]. Despite these improvements, TL show only a moderate electro-optical efficiency of $\eta < 50\,\%$ and are susceptible to a

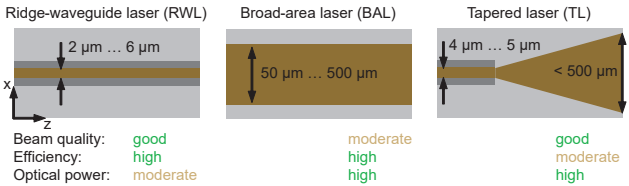

Figure 1.2: Schematic top view of a ridge-waveguide laser (RWL), a broad-area laser (BAL), and a tapered laser (TL). Underneath each laser type a rough classification in terms of beam quality, electro-optical efficiency, and optical output power is given.

power-dependent lateral astigmatism [31]. Astigmatism refers to different beam waist positions of the optical field diffracting in the lateral (x) and vertical (y) directions. However, the brightness achievable with TLs is higher than any other single emitter diode laser indicating the potential of lateral-longitudinal non-uniform laser designs to improve aspects of the device performance.

A further potential application of slightly tapered resonator designs, with an opening angle smaller than 4° to 6° as commonly used in TLs, is to reduce longitudinal spatial hole burning which is a direct result of lasers with asymmetric facet reflectivity values as commonly used in high-power diode lasers [33, 34]. However, lateral-longitudinal non-uniform laser designs are not restricted to high-power lasers. In recent years an increasing number of complex and highly functional lasers have been reported. This development was mainly driven by the demands of the telecom and datacom industry and therefore located at around 1550 nm emission wavelength. An example of highly integrated and functional devices are integrated dual-wavelength lasers which emit two distinct wavelengths out of a single waveguide aperture. The resulting beat note is mainly used to generate electrical signals in the microwave region [23, 35].

However, applications in spectroscopy as well as, the generation of terahertz radiation via GaAs-based photomixers, require dual-wavelength laser in the wavelength region covered by GaAs-based laser devices [35,36]. Consequently, Y-branch distributed Bragg reflector (DBR) dual-wavelength lasers centered at various wavelengths between 532 nm and 975 nm have been developed and successfully applied [37,38]. Nevertheless, these lasers have the potential to be further optimized in terms of compactness and functionality, output power, beam quality, and spectral stability.

Aim and structure of this thesis

In this thesis, various lateral-longitudinal non-uniform cavity designs for CW-driven edge-emitting GaAs diode lasers were investigated in detail. The aim was to improve selected performance parameters such as optical output power, beam quality, brightness, electro-optical efficiency, and spectral stability compared to currently used designs. This was done on the basis of passive waveguide and active laser simulations. Whenever possible the simulation results were compared to those of experiments.

This study was carried out on three different types of lasers, including dual-wavelength lasers with narrow and complex-shaped waveguides, tapered ridge-waveguide lasers, and tapered broad-area lasers, all of which are depicted schematically in Fig. 1.3. This

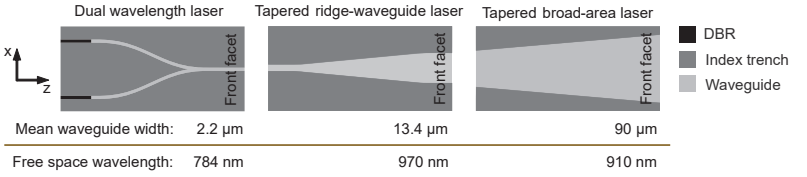

Figure 1.3: Schematic top view of the three investigated lateral-longitudinal non-uniform laser cavity designs. In addition, the corresponding mean waveguide widths and emission wavelengths are summarized at the bottom.

figure also highlights the differences in the corresponding ridge widths and emission wavelengths. A detailed introduction to each of these laser designs is given at the beginning of the corresponding chapters.

However, before presenting the results, the two preceding chapters provide a theoretical background on selected topics useful for understanding the present work. In Chapter 2, the fundamentals of wave propagation in dielectric waveguides are introduced, including longitudinally invariant integrated waveguide components, namely, waveguide bends, tapers, and couplers. The mathematical models of the used simulation tools are outlined in Chapter 3. This includes a two-dimensional (x-z) time-domain traveling wave modal-based laser simulator and an eigenmode expansion method-based three-dimensional Maxwell solver used to simulate and optimize integrated waveguide components.

In Chapters 4-6, the results of this thesis are presented. It starts with the presentation of a novel dual-wavelength laser in Chapter 4. It is aimed to avoid the shortcomings of previous Y-coupler-based laser designs, which suffer from strongly modulated near and far-field profiles as well as beam steering. This is followed by two chapters investigating the impact of tapered contact and waveguide layouts of ridge-waveguide and broad-area lasers. The focus in Chapter 5 is to increase the output power by keeping a good beam quality to reach very high brightness values. Chapter 6 is mainly about the impact of tapered broad-area laser designs on device efficiency as well as the intra-cavity intensity, carrier density, and temperature distributions.

Finally, in Cheaper 7, this work is summarized, and an outlook is given. The latter includes ideas on how to use the results of this work for future laser designs. Parts of the results presented in this thesis have already been published in Refs. [39–43].

Chapter 2

Wave propagation in optical waveguides

In this chapter, the theoretical basis for describing the light propagation in longitudinal non-uniform diode laser waveguide structures is introduced. For further details about optical waveguiding in diode lasers and photonic integrated circuits the reader is referred to Refs. [44–51].

The basis of dielectric waveguides is the effect of total internal reflection at the boundary of materials having different refractive indices n_1 and n_2 with $n_1 > n_2$, see Fig. 2.1. Light which propagates under the angle θ within a waveguide core gets completely reflected if $\theta < \theta_c = \arccos(n_2/n_1)$, with n_1 and n_2 being the waveguide core and cladding indices, respectively. However, not every angle θ leads to a lossless waveguide propagation since the accumulated phase has to fulfill the following eigenvalue equation

$$\frac{2\pi}{\lambda_0} n_1 h \sin(\theta^{(m)}) = \Phi(\theta^{(m)}) + \pi m \tag{2.1}$$

with λ_0, h, and $m = 1, 2, 3, ...$ being the free space wavelength, waveguide height and the number of the eigenvalue, respectively. Here, Φ takes into account the phase-shift due to the total internal reflection.

2.1 Maxwell's and wave equations

The classical behavior of electromagnetic fields inside arbitrarily shaped waveguides are governed by Maxwell's equations. Restricting its use to non-magnetizable materials and optical frequencies Maxwell's equations can be written in differential form as

$$\nabla \times \tilde{\boldsymbol{E}} = -\mu_0 \partial_t \tilde{\boldsymbol{H}}, \tag{2.2}$$

$$\nabla \times \tilde{\boldsymbol{H}} = \tilde{\tilde{\boldsymbol{j}}} + \partial_t \tilde{\boldsymbol{D}}, \tag{2.3}$$

$$\nabla \cdot \tilde{\boldsymbol{D}} = 0, \tag{2.4}$$

$$\nabla \cdot \tilde{\boldsymbol{H}} = 0, \tag{2.5}$$

where $\tilde{\tilde{\boldsymbol{j}}}$, $\tilde{\boldsymbol{E}}$, $\tilde{\boldsymbol{H}}$ and $\tilde{\boldsymbol{D}}$ are the time t and space $r = (x, y, z)$ dependent macroscopic current density, electric field, magnetic field and displacement field vectors, respectively.

The latter takes into account the material response to the E-field via

$$\tilde{\boldsymbol{D}} = \epsilon_0 \tilde{\boldsymbol{E}} + \tilde{\boldsymbol{P}} \tag{2.6}$$

with $\tilde{\boldsymbol{P}}$ being the dielectric polarization.

In general, Eqs. (2.2)-(2.6) are sufficient to model the propagation of light waves inside arbitrary dielectric waveguides. However, a more practical approach is to derive a wave equation for either the electric or the magnetic field. For the E-field this is done by applying $\nabla\times$ to Eq. (2.2) and using Eq. (2.3) to eliminate the H-field. Subsequently, the vector identity $\nabla \times \nabla \times \tilde{\boldsymbol{E}} = \nabla(\nabla \cdot \tilde{\boldsymbol{E}}) - \nabla^2 \tilde{\boldsymbol{E}}$ as well as Eq. (2.4) and Eq. (2.6) are used to obtain

$$\frac{1}{\varepsilon_0}\nabla(\nabla \cdot \tilde{\boldsymbol{P}}) + \nabla^2 \tilde{\boldsymbol{E}} = \mu_0 \partial_t \tilde{\boldsymbol{j}} + \frac{1}{c_0^2}\partial_t^2 \tilde{\boldsymbol{E}} + \mu_0 \partial_t^2 \tilde{\boldsymbol{P}}, \tag{2.7}$$

with ϵ_0, μ_0 and $c_0 = (\epsilon_0\mu_0)^{-1/2}$ being the free space permittivity, permeability and speed of light, respectively. The material response to the electric field leads to the polarization $\tilde{\boldsymbol{P}}$ which depends on the electric field history $\tilde{\boldsymbol{E}}(r, t-\tau)$ for $\tau > 0$ and is described by the convolution

$$\tilde{\boldsymbol{P}}(r,t) = \varepsilon_0 \int_0^\infty \chi(r,\tau)\tilde{\boldsymbol{E}}(r, t-\tau)\mathrm{d}\tau \tag{2.8}$$

with $\chi = \epsilon - 1$ being the susceptibility function and ϵ the relative permittivity. Using the convolution theorem, Eq. (2.8) can be written as the product $\boldsymbol{P}(r,\omega) = \varepsilon_0\chi(r,\omega)\boldsymbol{E}(r,\omega)$ in frequency space. The corresponding frequency domain wave equation can be obtained by applying the Fourier differentiation rule ($\partial_t \to \mathrm{i}\omega$) to Eq. (2.7) which leads to

$$\frac{1}{\varepsilon_0}\nabla(\nabla \cdot \boldsymbol{P}) + \nabla^2 \boldsymbol{E} = \mathrm{i}\omega\mu_0 \boldsymbol{j} - k_0^2 \boldsymbol{E} - \omega^2 \mu_0 \boldsymbol{P}. \tag{2.9}$$

Here, $k_0 = \frac{2\pi}{\lambda_0}$ and ω are the free space propagation constant and angular frequency, respectively. The bold letters without superscript tilde represent space and frequency dependent vectors. With the frequency domain equivalent of Eq. (2.6), neglecting the current term and by assuming that $\sqrt{\epsilon(r)} = n(r)$, Eq. (2.9) can be rewritten into

$$\nabla\left(\frac{\nabla n^2}{n^2}\boldsymbol{E}\right) + \nabla^2 \boldsymbol{E} = -k_0^2 n^2 \boldsymbol{E}. \tag{2.10}$$

If, in addition, the refractive index distribution $n(r)$ changes slowly on the wavelength scale then the first term on the left hand side of Eq. (2.10) is neglectable which leads to

$$\nabla^2 \Psi = -k_0^2 n^2 \Psi \tag{2.11}$$

known as scalar Helmholtz equation for inhomogeneous media. Here, the different E-field components are no longer coupled to each other and can all be represented separately by the scalar potential Ψ.

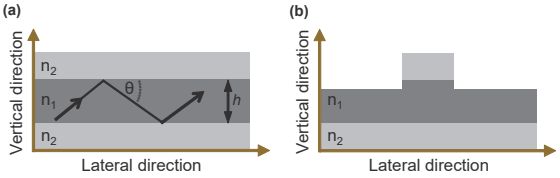

Figure 2.1: Schematic representation of (a) a vertical slab waveguide with n_1 and n_2 being the waveguide core and cladding refractive indices, respectively. Panel (b) shows a RW which can be formed by selectively removing parts of the slab waveguide.

2.2 Waveguide modes

The most simple optical waveguide is a slab waveguide as depicted in Fig. 2.1 (a). Here, light is only guided in one direction. In the context of diode lasers, this is the case for the epitaxially grown vertical waveguide consisting of layers having different refractive indices due to their specific material composition. However, the refractive index profile is normally more elaborated than shown here. An additional lateral optical confinement can be obtained by etching a pair of trenches which form a ridge waveguide (RW) as shown in Fig. 2.1 (b).

The propagation of monochromatic light waves inside arbitrarily shaped waveguide structures is fully governed by the wave equation (2.9). However, if the waveguide can be assumed to be longitudinal invariant, lets say in the z-direction, its mathematical description can be further simplified. The refractive index distribution $n(x, y, z)$ becomes $n(x, y)$ which allows to write the electrical field as

$$\mathbf{E}(x, y; z) = \mathbf{E}^{(m)}(x, y)\mathrm{e}^{-\mathrm{i}\beta^{(m)}z} = \begin{pmatrix} E_x^{(m)}(x, y) \\ E_y^{(m)}(x, y) \\ E_z^{(m)}(x, y) \end{pmatrix} \mathrm{e}^{-\mathrm{i}\beta^{(m)}z} \tag{2.12}$$

where $\beta^{(m)}$ is the complex modal propagation constant accounting for the phase and amplitude changes caused by the waveguide structure. Inserting Eq. (2.12) into the wave Eq. (2.10) leads to the following three equations [47]:

$$\begin{aligned} &\frac{\partial^2 E_x^{(m)}}{\partial y^2} + \frac{\partial}{\partial x}\left(\frac{1}{n^2}\frac{\partial\left(n^2 E_x^{(m)}\right)}{\partial x}\right) + \left(k_0^2 n^2 - (\beta^{(m)})^2\right) E_x^{(m)} \\ &\quad + \frac{\partial}{\partial x}\left(\frac{1}{n^2}\frac{\partial\left(n^2 E_y^{(m)}\right)}{\partial y}\right) - \frac{\partial^2 E_y^{(m)}}{\partial x \partial y} = 0, \end{aligned} \tag{2.13}$$

$$\begin{aligned} &\frac{\partial^2 E_y^{(m)}}{\partial x^2} + \frac{\partial}{\partial y}\left(\frac{1}{n^2}\frac{\partial\left(n^2 E_y^{(m)}\right)}{\partial y}\right) + \left(k_0^2 n^2 - (\beta^{(m)})^2\right) E_y^{(m)} \\ &\quad + \frac{\partial}{\partial y}\left(\frac{1}{n^2}\frac{\partial\left(n^2 E_x^{(m)}\right)}{\partial x}\right) - \frac{\partial^2 E_x^{(m)}}{\partial y \partial x} = 0, \end{aligned} \tag{2.14}$$

and

$$\begin{aligned}&\frac{\partial^2 E_z^{(m)}}{\partial x^2}+\frac{\partial^2 E_z^{(m)}}{\partial y^2}+\left(k_0^2 n^2-(\beta^{(m)})^2\right)E_z^{(m)}\\&-\mathrm{i}\beta^{(m)}\left(\frac{1}{n^2}\frac{\partial n^2}{\partial x}E_x^{(m)}+\frac{1}{n^2}\frac{\partial n^2}{\partial y}E_y^{(m)}\right)=0.\end{aligned}\tag{2.15}$$

Since Eq. (2.13) and Eq. (2.14) only contain transverse field components E_x and E_y it is sufficient to solve these equations defining the transverse field $\mathbf{E}_t=(E_x,E_y,0)$. If necessary, the $E_z^{(m)}$ and all $H^{(m)}$-field components can be calculated using Maxwell's equations.

The waveguide problem can be further simplified by assuming that the waveguide modes are either dominated by E_x and H_y (x-polarized) or by E_y and H_x (y-polarized) field components. This polarization approximation has proven to be quite accurate in the context of planar waveguide analysis [52]. It leads to two decoupled eigenvalue equations for the x-polarized quasi-TE modes

$$\frac{\partial^2 E_x^{(m)}}{\partial y^2}+\frac{\partial}{\partial x}\left(\frac{1}{n^2}\frac{\partial\left(n^2 E_x^{(m)}\right)}{\partial x}\right)+\left(k_0^2 n^2-(\beta^{(m)})^2\right)E_x^{(m)}=0\tag{2.16}$$

and y-polarized quasi-TM modes

$$\frac{\partial^2 E_y^{(m)}}{\partial x^2}+\frac{\partial}{\partial y}\left(\frac{1}{n^2}\frac{\partial\left(n^2 E_y^{(m)}\right)}{\partial y}\right)+\left(k_0^2 n^2-(\beta^{(m)})^2\right)E_y^{(m)}=0.\tag{2.17}$$

In the context of slab waveguides, as schematically shown in Fig. 2.1 (a), the refractive index distribution is invariant in one additional transverse direction. If this happens to be the lateral (x) direction the corresponding derivatives can be neglected leading to

$$\frac{\mathrm{d}^2 E_x^{(m)}}{\mathrm{d}y^2}+\left(k_0^2 n^2-(\beta^{(m)})^2\right)E_x^{(m)}=0\tag{2.18}$$

and

$$\frac{\mathrm{d}}{\mathrm{d}y}\left(\frac{1}{n^2}\frac{\mathrm{d}\left(n^2 E_y^{(m)}\right)}{\mathrm{d}y}\right)+\left(k_0^2 n^2-(\beta^{(m)})^2\right)E_y^{(m)}=0.\tag{2.19}$$

As outlined in Appendix B it is straight forward to numerically solve Eqs. (2.18) and (2.19) for arbitrary index profiles by using the finite-difference method. However, for piecewise homogeneous waveguides the equations can be solved analytically [45,47]. By assuming a symmetric slab waveguide with n_1 and n_2 being the core and cladding index, respectively, an expression for the number of guided slab modes M can be derived as [45]

$$M=\mathrm{ceil}\left(\frac{2h}{\lambda_0}\sqrt{n_1^2-n_2^2}\right)\tag{2.20}$$

where the ceil(x) function rounds its argument x to the next higher integer and h the waveguide core height as shown in Fig. 2.1.